







External Inverse-Compton Emission from Low-luminosity Gamma-Ray Bursts: Application to GRB 190829A

B. Theodore Zhang^{1,2,3} , Kohta Murase^{1,2,3,4} , Péter Veres⁵ , and Péter Mészáros^{1,2,3} 

¹Department of Physics, Pennsylvania State University, University Park, PA 16802, USA; bzz25@psu.edu

²Department of Astronomy & Astrophysics, Pennsylvania State University, University Park, PA 16802, USA

³Center for Multimessenger Astrophysics, Institute for Gravitation and the Cosmos, Pennsylvania State University, University Park, PA 16802, USA

⁴Center for Gravitational Physics, Yukawa Institute for Theoretical Physics, Kyoto University, Kyoto, Kyoto 606-8502, Japan

⁵Center for Space Plasma and Aeronomic Research (CSPAR), University of Alabama in Huntsville, Huntsville, AL 35899, USA

Received 2020 December 18; revised 2021 June 16; accepted 2021 June 19; published 2021 October 12

Abstract

The detection of TeV gamma-ray bursts (GRBs) brought new opportunities for studying the physics of particle acceleration at relativistic shocks. The High Energy Stereoscopic System (H.E.S.S.) telescopes recently observed very-high-energy (VHE) emission from a nearby low-luminosity GRB, GRB 190829A. Follow-up observations with, e.g., Swift-XRT, revealed unusual flare activities at $\sim 10^3$ s, which can be caused by a long-lasting central engine. We show that the VHE emission during the H.E.S.S. observation time is naturally produced in the external inverse-Compton (EIC) scenario, where seed photons supplied by the flares or other late-time dissipations are upscattered to VHE energies by the nonthermal electrons accelerated at the external forward shock. Our calculations show that the EIC flare nearly coincides with the late-prompt flare, but extends ~ 3 – 4 times longer than the duration of the late-prompt flare. The preferred kinetic energy and initial Lorentz factor used in our model are $\sim 10^{52}$ erg and ~ 20 , respectively. Understanding the mechanisms of the VHE emission from low-luminosity GRBs will help us constrain the properties of the outflow and the central engine activities, as well as the particle acceleration mechanism.

Unified Astronomy Thesaurus concepts: [Stellar jets \(1607\)](#); [Gamma-ray bursters \(1878\)](#); [X-ray sources \(1822\)](#); [Non-thermal radiation sources \(1119\)](#); [Radio sources \(1358\)](#); [Particle astrophysics \(96\)](#)

1. Introduction

Very-high-energy (VHE) γ -rays (γ -rays with energy greater than ~ 100 GeV) have been observed by ground-based Cherenkov telescopes (e.g., Hinton & Hofmann 2009; Inoue et al. 2013). The sources of VHE γ -rays represent extreme astrophysical accelerators in the universe. In the multimessenger era, the detection of VHE γ -rays along with multiwavelength electromagnetic radiation, neutrinos, cosmic rays, as well as gravitational waves can help to unveil the mechanisms of high-energy astrophysical processes (e.g., Mészáros et al. 2019; Murase & Bartos 2019).

The recent detection of two TeV gamma-ray bursts (GRBs), GRB 190114C (Acciari et al. 2019a, 2019b) and GRB 180720B (Abdalla et al. 2019), has opened a new window for studying GRBs in the VHE band, providing us with new opportunities to investigate the acceleration and radiation processes (see Mészáros 2006; Kumar & Zhang 2014, for reviews). VHE γ -rays originating from GRBs can be naturally explained with the inverse-Compton (IC) process by relativistic electrons (Mészáros & Rees 1994; Dermer et al. 2000; Sari & Esin 2001; Zhang & Mészáros 2001). The origins of VHE γ -rays from GRB 190114C and GRB 180720B have been widely discussed in the framework of the synchrotron self-Compton (SSC) scenario (Abdalla et al. 2019; Derishev & Piran 2019; Fraija et al. 2019; Wang et al. 2019; Zhang et al. 2020; Acciari et al. 2019b; Asano et al. 2020), where the same population of electrons that emit synchrotron photons can also upscatter these photons to much higher energies by a factor of $\sim \gamma_e^2$, where γ_e is the electron Lorentz factor (Blumenthal & Gould 1970; Rybicki et al. 1986).

Recently, the High Energy Stereoscopic System (H.E.S.S.) reported the detection of VHE γ -rays from GRB 190829A with

a confidence level of $>5\sigma$ (de Naurois 2019). The measured redshift of GRB 190829A is $z = 0.0785 \pm 0.005$ (Valeev et al. 2019), which is the nearest GRB detected in the VHE band. GRB 190829A has been discussed as a possible low-luminosity GRB (LL GRB), which has an isotropic-equivalent luminosity of $L_{\text{iso}} \sim 10^{49}$ erg s^{-1} (Chand et al. 2020). The late-time optical observation revealed an associated broad-line type-Ic supernovae, SN 2019oyw (Hu et al. 2021). Even though the physical origin of LL GRBs is still controversial, there is a consensus that LL GRBs are related to the deaths of massive stars and have properties between classical GRBs and normal supernovae (Kumar & Zhang 2014). The observed X-ray light curve indicates an unusual long-lasting flare during the time interval $\sim 10^2$ – 10^4 s, which may originate from a late-time central engine activity (Chand et al. 2020).

It has been proposed that VHE γ -rays can also be produced via the external inverse-Compton (EIC) process in the framework of GRBs, where the seed photons (produced in a region different from the acceleration zone) can be X-ray flares (Wang et al. 2006; He et al. 2012), late-time long-lasting emission (Murase et al. 2011, 2018; Veres & Mészáros 2012), prompt emission (Murase et al. 2010), shock breakout emission (Wang & Mészáros 2006), hypernova envelope emission (He et al. 2009), and cocoon emission (Toma et al. 2009; Kimura et al. 2019). If the long-lasting X-ray flare photons in GRB 190829A catch up with nonthermal electrons accelerated at the external forward shock, then these lower-energy photons can be upscattered to the VHE band. In the case of anisotropic scattering with target photons impinging from behind, the EIC flux of VHE γ -rays is reduced by a factor of 2 or 3 compared to the simplest estimate by the product of the scattering optical depth and seed photon flux (Brunetti 2000; Fan et al. 2008; Murase et al. 2011). However, if the target

photons have a larger energy density compared to synchrotron photons as in the case of late-time flares, then VHE γ -rays from the EIC emission can be dominant.

In this work, we study the origin of VHE γ -rays in the EIC scenario, with an application to GRB 190829A. The paper is organized as follows. In Section 2, we analytically discuss the origin of high-energy emission considering both the SSC and EIC scenarios in the framework of GRB 190829A. In Section 3, we show the numerical results and make a comparison to observations. We discuss the implications of this work and give a summary in Section 5. Throughout the paper, we use cgs units, and adopt notations such as $Q_x \equiv Q/10^x$. We use E to represent observed photon energy, $\varepsilon = E(1+z)$ is the photon energy measured in the cosmic rest frame, and $\varepsilon' = \varepsilon/\Gamma$ is the photon energy measured in the source comoving frame, which has Lorentz factor Γ .

2. High-energy Afterglow Emission from GRBs

We consider a relativistic outflow that has isotropic-equivalent energy \mathcal{E}_k and initial Lorentz factor Γ_0 , propagating into an external medium with constant density n_{ex} . In this work, we numerically calculate afterglow dynamics in detail for both relativistic and nonrelativistic regimes. However, in the following text, we mainly discuss the results using the self-similar evolution phase of the adiabatic blast wave (Blandford & McKee 1976) to explain essential results. We numerically calculate EIC emission following Murase et al. (2010) and Murase et al. (2011), and we perform numerical calculations for synchrotron emission as well.

The radius of the forward shock is estimated to be

$$R \simeq 2.2 \times 10^{17} \mathcal{E}_{k,52}^{1/4} n_{\text{ex}}^{-1/4} t_{z,4}^{1/4} \text{ cm}, \quad (1)$$

where $t_{z,4} = t_4/(1+z)$ is the redshift-corrected observation time and the bulk Lorentz factor is

$$\Gamma \simeq 14 \mathcal{E}_{k,52}^{1/8} n_{\text{ex}}^{-1/8} t_{z,4}^{-3/8}, \quad (2)$$

where the relation between radius R and observation time t is $R \approx 4\Gamma^2 ct_z$ which takes into account the history of the blast wave evolution and the contribution from a range of angles within $1/\Gamma$ cone (Waxman 1997; Panaitescu & Mészáros 1998; Sari et al. 1998).

In the external forward shock model, a fraction of thermal electrons can be injected into the acceleration process and is able to accelerate to higher energies via the diffusive shock acceleration mechanism (e.g., Drury 1983; Blandford & Eichler 1987). The lower-energy synchrotron photons and external photons can then be upscattered to the VHE band by high-energy nonthermal electrons. The luminosity of the newly accelerated electrons can be estimated to be $L_e \sim \epsilon_e 4\pi R^2 c \Gamma^2 U'_{\text{sh}} \sim 2 \times 10^{47} \epsilon_{e,-1} \mathcal{E}_{k,52} t_{z,4}^{-1} \text{ erg s}^{-1}$, where ϵ_e is the fraction of internal energy that goes into shocked electrons and $U'_{\text{sh}} \sim 2\Gamma^2 n_{\text{ex}} m_p c^2$ is the comoving internal energy density (Wang et al. 2006; Fan et al. 2008). We approximate the synchrotron luminosity to be

$$L_{\text{syn}} \sim \frac{1}{1 + Y_{\text{tot}}} \zeta_\gamma L_e, \quad (3)$$

where ζ_γ is the fraction of electron energy that is radiated, $Y_{\text{tot}} = Y_{\text{SSC}} + Y_{\text{EIC}}$ is the total Compton parameter, Y_{SSC} is the SSC Compton parameter defined as the ratio between the SSC

luminosity and the synchrotron luminosity, and Y_{EIC} is the EIC Compton parameter defined as the ratio between the EIC luminosity and the synchrotron luminosity. In the fast-cooling regime, the value of ζ_γ equals 1, while in the slow cooling regime $\zeta_\gamma \sim (\gamma_{e,c}/\gamma_{e,m})^{2-s}$ where s is the electron spectral index (Sari & Esin 2001). The minimum electron Lorentz factor is

$$\begin{aligned} \gamma_{e,m} &\approx (\epsilon_e/f_e) g(s) (m_p/m_e) (\Gamma - 1) \\ &\sim 400 \mathcal{E}_{k,52}^{1/8} n_{\text{ex}}^{-1/8} \epsilon_{e,-1} f_e^{-1} t_{z,4}^{-3/8}, \end{aligned} \quad (4)$$

where ϵ_e is the energy fraction of internal energy that goes into electrons and f_e is the number fraction of electrons that are accelerated, and $g(s) = (s-2)/(s-1)$ for $s > 2$ (we adopt $s = 2.2$). The maximum electron Lorentz factor is limited by the cooling process,

$$\begin{aligned} \gamma_{e,M} &\approx (6\pi e / (\sigma_T B \eta (1 + Y_{\text{tot}})))^{1/2} \\ &\sim 9 \times 10^8 \eta^{-1/2} (1 + Y_{\text{tot}})^{-1/2} \mathcal{E}_{k,52}^{-1/16} n_{\text{ex}}^{-3/16} \epsilon_{B,-5}^{-1/4} t_{z,4}^{3/16}, \end{aligned} \quad (5)$$

where η is the acceleration efficiency, which depends on details of the acceleration mechanism (see, e.g., Equation (14) of Asano et al. 2020), and ϵ_B is the energy fraction of internal energy that is converted into the magnetic energy. The electron cooling Lorentz factor is,

$$\begin{aligned} \gamma_{e,c} &\approx \frac{6\pi m_e c}{(1 + Y_{\text{tot}}) \sigma_T \Gamma B^2 t_z} \\ &\sim 2 \times 10^7 (1 + Y_{\text{tot}})^{-1} \mathcal{E}_{k,52}^{-3/8} n_{\text{ex}}^{-5/8} \epsilon_{B,-5}^{-1} t_{z,4}^{1/8}. \end{aligned} \quad (6)$$

The nonthermal electrons are in the fast-cooling regime for $\gamma_{e,m} > \gamma_{e,c}$, where nearly all of the injected electrons cool during the dynamical time. When $\gamma_{e,m} < \gamma_{e,c}$, electrons are in the slow cooling regime. Note in the following analytical estimates, we mainly consider the slow cooling regime, while our numerical code can treat both slow- and fast-cooling cases self-consistently. Note that the fraction of electron energy that was radiated away in the slow cooling case is estimated to be $\zeta_\gamma \sim 0.1(1 + Y_{\text{tot}})^{s-2} \mathcal{E}_{k,52}^{-\frac{2-s}{2}} n_{\text{ex}}^{-\frac{2-s}{2}} \epsilon_{B,-5}^{s-2} \epsilon_{e,-1} f_e^{2-s} t_{z,4}^{\frac{2-s}{4}}$. The characteristic energy of the synchrotron emission is estimated to be $E_m \approx [eB/(2\pi m_e c)] \gamma_m^2 \Gamma / (1+z) \simeq 4.2 \times 10^{-4} \mathcal{E}_{k,52}^{1/2} \epsilon_{e,-1}^2 f_e^{-2} \epsilon_{B,-5}^{1/2} t_{z,4}^{-3/2} (1+z)^{1/2} \text{ eV}$ and the corresponding cooling energy is $E_c \approx [eB/(2\pi m_e c)] \gamma_c^2 \Gamma / (1+z) \simeq 10^6 (1 + Y_{\text{tot}})^{-2} \mathcal{E}_{k,52}^{-1/2} n_{\text{ex}}^{-1} \epsilon_{B,-5}^{-3/2} t_{z,4}^{-1/2} (1+z)^{-1/2} \text{ eV}$. The observed X-ray luminosity at the keV band will evolve as $L_X \propto t^{(3-3s)/4}$ for $E_m < E_X < E_c$ (Zhang et al. 2006).

The SSC luminosity can be estimated as

$$L_{\text{SSC}} \sim \frac{Y_{\text{SSC}}}{1 + Y_{\text{tot}}} \zeta L_e. \quad (7)$$

Note that $\epsilon_e \gg \epsilon_B$ is one of the conditions for dominant SSC emission (Sari et al. 1998; Zhang & Mészáros 2001). In the Thomson limit, the value of Y_{SSC} remains constant as a function of γ_e (Sari & Esin 2001), and the SSC luminosity will

evolve as $L_{\text{SSC}} \propto \zeta_\gamma L_e \propto t_z^{-s/2}$. Thus, we can expect that the SSC light curve will have a very similar trend as the X-ray light curve for $s > 2$. The characteristic energies of the SSC emission can be estimated as $E_m^{\text{SSC}} \approx 2\gamma_{e,m}^2 E_m \simeq 1.4 \times 10^2 \mathcal{E}_{k,52}^{3/4} \epsilon_{e,-1}^4 f_e^{-4} \epsilon_{B,-5}^{1/2} t_z^{-9/4} (1+z)^{-5/4}$ eV and $E_c^{\text{SSC}} \approx 2\gamma_{e,c}^2 E_c \simeq 9.5 \times 10^{20} (1+Y_{\text{tot}})^{-4} \mathcal{E}_{k,52}^{-5/4} n_{\text{ex}}^{-9/4} \epsilon_{B,-5}^{-7/2} t_z^{-1/4} (1+z)^{-3/4}$ eV. In the Thomson limit, the SSC energy spectrum in the slow cooling case is

$$F_E^{\text{SSC}} = F_{E,\text{max}}^{\text{SSC}} \begin{cases} \left(\frac{E}{E_m^{\text{SSC}}} \right)^{\frac{1}{3}}, & E < E_m^{\text{SSC}} \\ \left(\frac{E}{E_m^{\text{SSC}}} \right)^{-\frac{(s-1)}{2}}, & E_m^{\text{SSC}} < E < E_c^{\text{SSC}}, \\ \left(\frac{E_c^{\text{SSC}}}{E_m^{\text{SSC}}} \right)^{\frac{1-s}{2}} \left(\frac{E}{E_c^{\text{SSC}}} \right)^{-\frac{s}{2}}, & E > E_c^{\text{SSC}} \end{cases} \quad (8)$$

where $F_{E,\text{max}}^{\text{SSC}} \sim \tau_T F_{E,\text{max}}^{\text{syn}}$ and $\tau_T \sim (1/3)\sigma_T R n_{\text{ex}} f_e \sim 5 \times 10^{-8} \mathcal{E}_{k,52}^{1/4} n_{\text{ex}}^{3/4} f_e t_{z,4}^{1/4}$ is the electron scattering optical depth (Sari & Esin 2001). The peak synchrotron flux can be calculated as $F_{E,\text{max}}^{\text{syn}} \approx (1+z) N_e P_{\epsilon,\text{max}} / 4\pi d_L^2$ where $P_{\epsilon,\text{max}} \approx P(\gamma_{e,m}) / \epsilon_m = (c\sigma_T / 6\pi) \gamma_{e,m}^2 B^2 \Gamma^2 / \epsilon_m$ is the synchrotron emission power per electron (Sari et al. 1998) and $\epsilon_m = E_m(1+z)$.

Similarly, the EIC luminosity is

$$L_{\text{EIC}} \sim \frac{Y_{\text{EIC}}}{1+Y_{\text{tot}}} \zeta_\gamma L_e, \quad (9)$$

The EIC light curve depends on the time evolution of external photons. For prompt or flare photons as targets, the observed EIC light curve usually appears as an extended bump compared to the SSC light curve (Murase et al. 2010). On the other hand, for long-lasting photons as target photons, the EIC light curve is flatter than the SSC light curve, which may dominate at later times (Murase et al. 2011). Assuming that the external photons can be described as a broken power law with break energy E_b , then the characteristic energies of EIC emission are $E_m^{\text{EIC}} \approx 2\gamma_{e,m}^2 E_b \simeq 3.3 \times 10^7 \mathcal{E}_{k,52}^{1/4} n_{\text{ex}}^{-1/4} \epsilon_{e,-1}^2 f_e^{-2} t_z^{-3/4} (1+z)^{3/4} E_{b,2}$ eV and $E_c^{\text{EIC}} \approx 2\gamma_{e,c}^2 E_b \simeq 8.6 \times 10^{16} (1+Y_{\text{tot}})^{-1} \mathcal{E}_{k,52}^{-3/4} n_{\text{ex}}^{-5/4} \epsilon_{B,-5}^{-2} t_z^{1/4} (1+z)^{-1/4} E_{b,2}$ eV. We model the energy spectrum of the flare as a broken power law without going into the details of the emission mechanism,

$$F_E^{\text{fl}} = F_{E_b}^{\text{fl}}(t) \begin{cases} \left(\frac{E}{E_b} \right)^{-\alpha+1}, & E < E_b \\ \left(\frac{E}{E_b} \right)^{-\beta+1}, & E > E_b \end{cases}, \quad (10)$$

where E_b is the break frequency measured in the observer frame, $F_{E_b}^{\text{fl}}(t)$ is the peak flux at E_b , and α and β are the spectral indices. The energy spectrum of EIC emission in the Thomson

limit is

$$F_E^{\text{EIC}} = F_{E,\text{max}}^{\text{EIC}} \begin{cases} \left(\frac{E}{E_m^{\text{EIC}}} \right)^{1-\alpha}, & E < E_m^{\text{EIC}} \\ \left(\frac{E}{E_m^{\text{EIC}}} \right)^{-\frac{(s-1)}{2}}, & E_m^{\text{EIC}} < E < E_c^{\text{EIC}}, \\ \left(\frac{E_c^{\text{EIC}}}{E_m^{\text{EIC}}} \right)^{\frac{1-s}{2}} \left(\frac{E}{E_c^{\text{EIC}}} \right)^{-\frac{s}{2}}, & E > E_c^{\text{EIC}} \end{cases} \quad (11)$$

where $F_{E,\text{max}}^{\text{EIC}} \sim \tau_T x F_{E_b}^{\text{fl}}$, $F_{E_b}^{\text{fl}}$ is the peak flux of the late-prompt emission, and $x < 1$ is a factor due to the anisotropic scattering process (Murase et al. 2011).

The SSC (EIC) Compton parameter is expressed as the ratio of SSC (EIC) emission power to synchrotron emission power,

$$Y_{\text{SSC(EIC)}}(\gamma_e) \approx \frac{P_{\text{SSC(EIC)}}}{P_{\text{syn}}} \sim \frac{U'_{\text{syn(FL)}} [\epsilon' < \epsilon'_{\text{KN}}]}{U'_B}, \quad (12)$$

where P_{SSC} is the SSC emission power, P_{EIC} is the EIC emission power, P_{syn} is the synchrotron emission power, U'_{syn} is the comoving synchrotron photon energy density, where we introduce the Klein–Nishina energy $\epsilon'_{\text{KN}} \sim m_e c^2 / \gamma_e$ to take into account Klein–Nishina effect, U'_{FL} is the comoving photon density of flares, and $U'_B = B^2 / 8\pi$ is the comoving magnetic energy density. If we neglect EIC cooling, the value of Y_{SSC} can be estimated to be $Y_{\text{SSC}} \sim (\epsilon_e / \epsilon_B)^{1/(4-s)} (\gamma_{e,m} / \gamma_{c,\text{syn}})^{-(s-2)/(2(s-4))} \sim 90$ at $t \sim 10^4$ s in the Thomson regime (Sari & Esin 2001; Liu et al. 2013).

It has been shown that both the synchrotron spectrum and the SSC (EIC) spectrum can be affected in the Klein–Nishina regime (see, e.g., Nakar et al. 2009; Wang et al. 2010; Murase et al. 2011). The Klein–Nishina effect on the high-energy IC emission leads to the spectral suppression when the upscattered photons have energies beyond the critical energy (Blumenthal & Gould 1970). In the observer frame, the characteristic break energies are $E_{\text{KN}}^m \approx \Gamma \gamma_{e,m} m_e c^2 / (1+z) \simeq 2.9 \times 10^9 \mathcal{E}_{k,52}^{1/4} n_{\text{ex}}^{-1/4} \epsilon_{e,-1} f_e^{-1} t_{z,4}^{-3/4} (1+z)^{-1}$ eV and $E_{\text{KN}}^c \approx \Gamma \gamma_{e,c} m_e c^2 / (1+z) \simeq 1.5 \times 10^{14} (1+Y_{\text{tot}})^{-1} \mathcal{E}_{k,52}^{-1/4} n_{\text{ex}}^{-3/4} \epsilon_{B,-5}^{-1} t_z^{-1/4} (1+z)^{-1}$ eV. The Klein–Nishina break energy can be lower than either E_c^{SSC} or E_c^{EIC} . The energy spectrum in Equations (8) and (11) can be further affected by the Klein–Nishina effect, where the spectrum is steepened beyond the Klein–Nishina break energy (see Equations (24) and (25) of Murase et al. 2011).

This work focuses on the case in which EIC emission dominates over SSC emission because the peak flux of the flare emission is much larger than the afterglow synchrotron emission, i.e., $F_{E_b}^{\text{FL}} > F_{E,\text{max}}^{\text{syn}}$. However, the evolution of the blast wave may still be in the coasting phase during the stage of the flare emission. In our numerical calculations, we consider the coasting phase, deceleration phase and nonrelativistic phase by solving a series of partial differential equations. See Appendix A for details. Note the emission during the nonrelativistic evolution phase is necessary for explaining the late-time radio data (Rhodes et al. 2020). By extending the method adopted in Murase et al. (2011), we numerically calculate spectra of synchrotron, SSC, and EIC

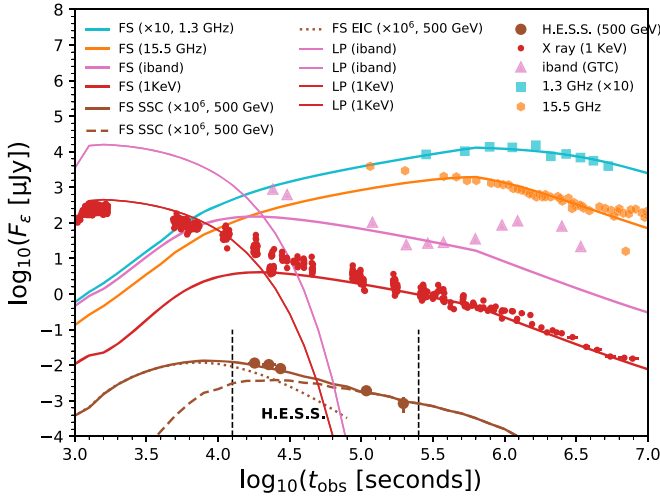


Figure 1. Multiwavelength light curve from radio, optical, and X-ray to TeV bands. We show both the forward shock (FS) light curve (thick lines) and the late-prompt (LP) light curve (thin lines). The H.E.S.S. observation time window is indicated within black dashed vertical lines. The relevant physical parameters are $\mathcal{E}_k = 9.8 \times 10^{51}$ erg, $n_{\text{ex}} = 0.09$ cm $^{-3}$, $\epsilon_e = 0.39$, $f_e = 0.34$, $\epsilon_B = 8.7 \times 10^{-5}$, $s = 2.1$, $\theta_j = 0.2$, $\Gamma_0 = 25$, $\alpha = 1$, $\beta = 2.5$, and $E_b = 100$ eV.

emission. We take into account the equal-arrival-time surface (EATS) for not only the EIC component but also the synchrotron and SSC components. See details in Appendix C.

3. Modeling High-energy Gamma-Ray Emission from GRB 190829A

Following Chand et al. (2020), we fit the observed X-ray light curve with two separate components, the late-time flare emission and external forward shock emission, respectively. The X-ray light curve drops very quickly during the flare stage, which is difficult to explain in the standard afterglow model with typical electron spectral indices of $s \sim 2$ –2.5. The late-time X-ray flare can be fitted with the Norris model (Norris et al. 2005; Chand et al. 2020),

$$F_{\mathcal{E}_b}^{\text{fl}}(t) = A\lambda e^{-\frac{\tau_1}{t-t_i} - \frac{t-t_i}{\tau_2}}, \quad (13)$$

where A is the pulse amplitude, t_i is the pulse start time, τ_1 is the pulse rise parameter, τ_2 is the pulse decay parameter, λ is defined as the normalization constant $\lambda = \exp[2(\tau_1/\tau_2)^{1/2}]$. The best-fit results of the above parameters are $A = 225$ μ Jy, $\tau_1 = 90$ s, $\tau_2 = 3993$ s, and $t_i = 950$ s. The corresponding values used in Equation (10) are $\alpha = 1$, $\beta = 2.5$, and $E_b = 100$ eV, which is optimized for brighter EIC fluxes.

In Figure 1, we show the multiwavelength light curve from radio, optical, and X-ray to VHE band. The X-ray light curve at 1 keV that has been observed by Swift-XRT is taken from the public online repository⁶ (Evans et al. 2010). We can see the observed X-ray flux is well explained with both contributions from the late-prompt flare and forward shock emission. Assuming the opening angle of the outflow is $\theta_j \sim 0.2$ radian, the jet break occurred at $t \sim 10^5$ s. Although there is a lateral expansion, the spectral decline after the jet break is known to be dominated by the geometrical effect, so we simply multiply a correction factor $\theta_j^2 \Gamma^2$ to the observed flux reduction after the jet break (Zhang 2018). The pink triangles are the optical

i-band data observed by the Gran Telescopio CANARIAS after the correction for both Galactic and host galaxy extinction (Hu et al. 2021). As done for X-rays, we fit the optical light curve as a combination of the late-prompt flare and external forward shock emission. Note that the bump that appeared in the late-time optical data should be attributed to supernova emission. We also show the radio data at 1.3 GHz band (yellow squares) and 15.5 GHz band (blue points) observed by MeerKAT Array Telescope (MeerKAT) and Arcminute Microkelvin Imager–Large Array (AMI-LA) one day after the burst, respectively (Rhodes et al. 2020). In our model, the radio light curve at 1.3 and 15.5 GHz can be explained in the external forward shock model, even though possible contributions may also come from the external reverse shock (Rhodes et al. 2020). Note that we include an additional parameter f_e in our model to consider the case where only a fraction of the electrons are injected into the acceleration process, which can affect the minimum electron Lorentz factor $\gamma_{e,m}$ as well as the flux at the radio band (Samuelsson et al. 2020).

We show the SSC and EIC light curves at 500 GeV as dashed and dotted lines, respectively. The EIC light curve dominates the high-energy emission at $t \sim 10^3$ – 10^4 s, and gradually declines due to the decrease of the late-prompt flare emission. The SSC light curve becomes dominant at later times, $t \gtrsim 3 \times 10^4$ s. We define θ'_{sc} as the scattering angle relative to the photon beam measured in the external forward shock comoving frame. The EIC emission diminishes at $\theta'_{\text{sc}} = 0$. See Appendix C for more details. The EIC emission nearly coincides with the late-prompt flare, but it extends a factor of ~ 3 –4 times longer than the duration of the flare (Murase et al. 2011). Despite the rapid evolution of the late-prompt flare, the EIC flux decreases slowly due to the effect of the integration over the EATS. Note that for a given time the angle at which nonthermal electrons produce the dominant fraction of the EIC flux is $\theta \lesssim \Gamma^{-1}$ (Murase et al. 2011), which is smaller than the jet opening angle θ_j before the jet break.

In Figure 2, we show energy spectra of various components including the flare, synchrotron, SSC, and EIC at $t = 3.5$ hr. The synchrotron emission peaks around $E_c \sim 10^6$ eV and the characteristic energy is $E_m \sim 10^{-1}$ eV. It is clear that the upscattering of these higher-energy photons is limited by the Klein–Nishina effect. The maximum EIC flux is observed at $t \sim 3.5$ hr with a peak flux of $\sim 10^{-10.5}$ erg cm $^{-2}$ s $^{-1}$. At the same time, the SSC flux is ~ 5 times lower than the EIC flux, as shown in Figure 2. The cutoff of the VHE emission at $\gtrsim 500$ GeV is dominated by the EBL attenuation during their propagation from the source to Earth. Note that the effect of the Klein–Nishina break energy is difficult to observe due to the strong EBL attenuation.

VHE γ -rays from GRB 190829A have been detected by H.E.S.S. with a confidence level $> 5\sigma$ (de Naurois 2019). The observations started at $\sim 1.5 \times 10^4$ s after the GRB trigger, where the integral flux beyond 200 GeV reached $\sim 4 \times 10^{11}$ erg cm $^{-2}$ s $^{-1}$ and gradually decline following the same trend as X-rays until $t \sim 2 \times 10^5$ s (Abdalla et al. 2021). Our calculations predict that the high-energy EIC emission has a flux of $\gtrsim 10^{-11}$ erg cm $^{-2}$ s $^{-1}$ consistent with the H.E.S.S. observation in the earlier observation time, while the late-time observation at $t \sim 10^5$ s can be explained by the SSC emission.

⁶ We convert the observed flux at 0.3–10 keV to that at 1 keV, assuming a spectral index of $\Gamma_X = 1.8$.

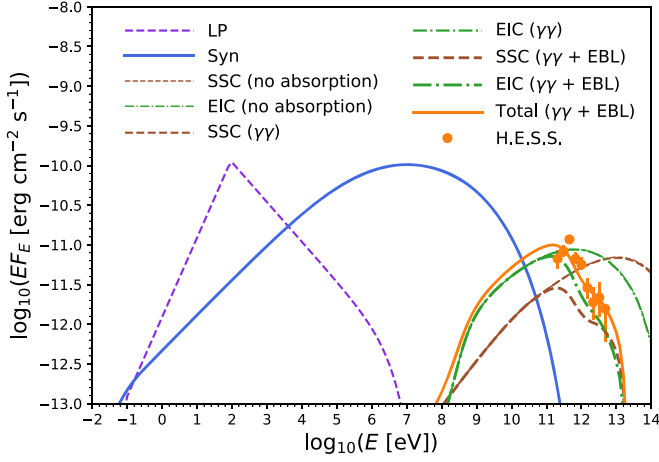


Figure 2. Same as Figure 1, we show energy spectra of the synchrotron, SSC, EIC, and late-prompt (LP) flare emission at $t = 4.4$ hr. The thick green, red, and yellow lines take into account both of the internal $\gamma\gamma$ absorption and EBL attenuation. The H.E.S.S. VHE spectra data on the first night are taken from Abdalla et al. (2021).

4. Discussion

VHE γ -rays from GRB 190829A have been studied based on the SSC scenario, as in other VHE GRBs (Chand et al. 2020; Fraija et al. 2021; Hu et al. 2021; Rhodes et al. 2020; Sato et al. 2021). However, the relative ratio of the EIC component to SSC component depends on both the energy spectrum of flare emission and synchrotron emission, $F_{E=500\text{GeV}}^{\text{EIC}}/F_{E=500\text{GeV}}^{\text{SSC}} = (F_{E_b}^{\text{II}}/F_{E_{\text{max}}}^{\text{syn}})(E_m/E_b)^{-(s-1)/2} \sim Y_{\text{EIC}}/Y_{\text{SSC}}$, which can be derived from Equations (8), (11), and (12). In Figure 3, we show the synchrotron cooling timescale t_{syn} , the SSC cooling timescale t_{SSC} , and the EIC cooling timescale t_{EIC} , as a function of γ_e at $t = 10^4$ s. We also show the time evolution of the Compton parameters, $Y_{\text{SSC}}(\gamma_e)$ and $Y_{\text{EIC}}(\gamma_e)$, at various observation times. We can see that $Y_{\text{SSC}}(\gamma_e)$ is not constant and it declines with the increase of γ_e due to the Klein–Nishina effect. According to Equation (12), the value of $Y_{\text{SSC}}(\gamma_e)$ is proportional to the comoving synchrotron photon energy density $U'_{\text{syn}}[\epsilon' < \epsilon'_{\text{KN}}] \propto \epsilon'_{\text{KN}}^{-1/2}$. Note ϵ'_{KN} is proportional to γ_e^{-1} , we can expect $Y_{\text{SSC}}(\gamma_e) \propto \gamma_e^{-1/2}$ consistent with $Y_{\text{SSC}}(\gamma_e)$ shown in Figure 3. Unlike $Y_{\text{SSC}}(\gamma_e)$, the Compton parameter $Y_{\text{EIC}}(\gamma_e)$ remains constant up to $\gamma_e \sim 10^5$. The reason is that the energy density of the late-prompt photons $U'_{\text{EIC}}[\epsilon' < \epsilon'_{\text{KN}}]$ remains constant, which is dominated by the energy density near $\epsilon_b \sim 100$ eV as long as $\gamma_e \lesssim 10^4$. One visible feature of $Y_{\text{EIC}}(\gamma_e)$ is the rapid decline following the time evolution of the X-ray flare.

The physical parameters of LL GRBs are still uncertain due to the limited number of observations and the values used in Figure 1 are optimized for fitting the multiwavelength light curve. The values of the microphysical parameters are $\epsilon_e \sim 0.4$, $f_e \sim 0.3$, and $\epsilon_B = 9 \times 10^{-5}$, assuming uniform microturbulence in the shock vicinity. For GRB afterglows, the typical value of ϵ_e is ~ 0.1 , while the value of ϵ_B varies in a wide range, e.g., $\sim 10^{-5}$ – 10^{-1} (Kumar & Zhang 2014). Small values of ϵ_B can be consistent with ones expected around the contact discontinuity, considering the decay of ϵ_B from a stronger value of ~ 0.01 at the shock front inferred from particle-in-cell simulations (Lemoine 2013; Vanthieghem et al. 2020).

In this work, we consider an impulsive relativistic outflow with a kinetic energy of $\mathcal{E}_k = 1 \times 10^{52}$ erg and an initial

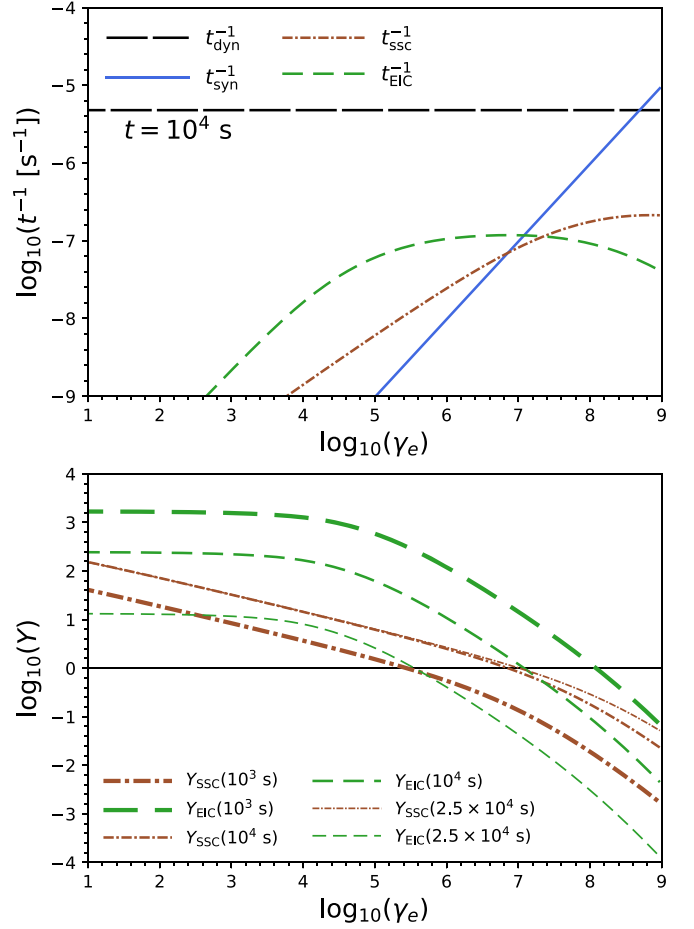


Figure 3. Upper panel: dynamical timescale and various electron cooling timescales for synchrotron, SSC, and EIC as a function of electron Lorentz factor γ_e . Lower panel: the evolution of $Y_{\text{SSC}}(\gamma_e)$ and $Y_{\text{EIC}}(\gamma_e)$ as a function of γ_e at $t = 10^3$ s, $t = 10^4$ s, and $t = 2.5 \times 10^4$ s.

Lorentz factor of $\Gamma_0 = 25$, propagating into an external medium with a constant density of $n_{\text{ex}} = 0.14 \text{ cm}^{-3}$. The value of kinetic energy and Γ_0 is larger than for LL GRBs, e.g., GRB 980425 (Galama et al. 1998; Kulkarni et al. 1998) and GRB 060218 (Campana et al. 2006; Soderberg et al. 2006), but smaller than canonical high-luminosity GRBs (Kumar & Zhang 2014). The value of Γ_0 should not be much smaller, e.g., $\Gamma < 10$, otherwise the deceleration time is too long. A higher value of $\Gamma_0 > 25$ will enhance the SSC contribution at earlier time $t \lesssim 10^4$ s, but the flux of VHE γ -rays is still dominated by EIC components. We stress that the advantage of the EIC+SSC model presented in this work is that in the presence of X-ray flares it gives a better fit to the multi-wavelength light curve with microphysical parameters that are similar to other TeV GRBs. In Figure 4, we show the time evolution of the Lorentz factor and radius of the blast wave. The deceleration time can be determined when the total mass of the swept-up matter equals a fraction $1/\Gamma_0$ of the ejecta mass, $R_{\text{dec}} \simeq 2.9 \times 10^{17} \epsilon_{k,52}^{1/3} \Gamma_{0,1.4}^{-2/3} n_{\text{ex},-1}^{-1/3} \text{ cm}$, and the corresponding deceleration time can be estimated to be $t_{\text{dec}} \approx (1+z)R_{\text{dec}}/2\Gamma_0 c^2 \simeq 8.4 \times 10^3 (1+z) \epsilon_{k,52}^{1/3} \Gamma_{0,1.4}^{-8/3} n_{\text{ex},-1}^{-1/3} \text{ s}$. In addition, we note that the predicted Lorentz factor of the ejecta is $\Gamma \sim 1.7$ at ~ 60 days, which is only slightly smaller than the velocity measured by the Very Long Baseline Interferometry (VLBI; Marcello 2021).

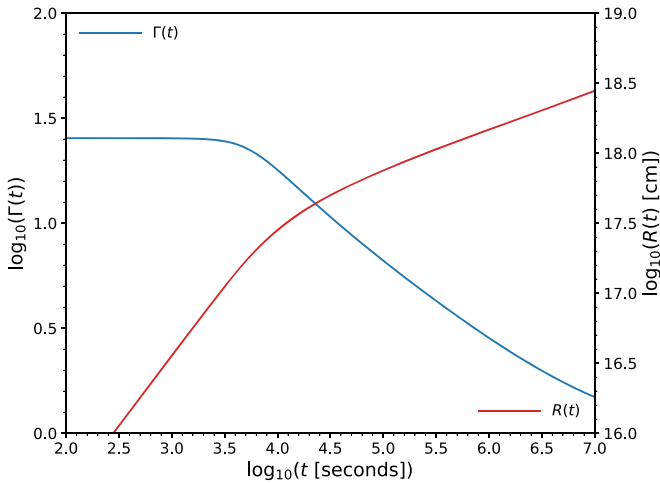


Figure 4. Time evolution of the Lorentz factor and radius of the blast wave as a function of the observation time since the burst, t .

Our results can also be affected by the energy spectrum of late-prompt emission. For example, the peak flux F_{ϵ_b} used in Equation (10) will decrease for a smaller value of β , given the constraints at the X-ray band. In this work, the break energy ϵ_b of the late-prompt flare emission is chosen to be constant. In general, the value of ϵ_b may decrease with time (Murase et al. 2011). However, the evolution of ϵ_b is not essential for our conclusions, since lower values of ϵ_b at later times can enhance the scattering efficiency in the Thomson regime when $\gamma_{e,c}$ becomes larger. Compared to canonical high-luminosity GRBs, energy spectra of LL GRBs usually have lower ϵ_m and higher ϵ_c , with the dominance of photons with energies around ϵ_c . The Klein–Nishina effect in the SSC spectrum will be more relevant in such a situation. The IC scattering between the same population of electrons with external photons can alleviate the Klein–Nishina suppression if the external photons have the proper energies that can keep the IC scattering process in the Thomson regime.

GRB 190829A has the lowest radio luminosity in the GRB samples considered in Rhodes et al. (2020). However, there is no difference in the radio luminosity among all of the three VHE GRBs and other GRBs. The associated supernova SN 2019oyw appeared to have similar ejecta mass and kinetic energy as SN 1998bw (Hu et al. 2021) that was associated with an LL GRB. Note that thermal photons from an associated supernova can also be upscattered by nonthermal high-energy electrons accelerated by the conventional GRB outflow or trans-relativistic ejecta (Ando & Mészáros 2008; Asano & Mészáros 2008; He et al. 2009). Hadronic VHE γ -rays from LL GRBs have also been studied. In particular, Murase et al. (2008) and Murase & Beacom (2010) proposed heavy-ion synchrotron emission and VHE γ -rays from the deexcitation of the UHECR nuclei, respectively (see, e.g., Figure 9 of Murase et al. 2008). On the other hand, Murase (2012) and Kashiyama et al. (2013) suggested hadronic VHE γ -rays originating from $p\gamma$ interactions following prompt and shock breakout emission, respectively. These mechanisms would compete with high-energy emission from primary electrons (Ando & Mészáros 2008). The detailed modeling of the hadronic processes and the following electromagnetic cascade is essential (see, e.g., Murase & Beacom 2010, as an example of hadronic and leptonic components) to disentangle the hadronic component from the leptonic component and to obtain constraints both

on cosmic-ray acceleration mechanisms and on radiation processes.

5. Summary

In this work, we showed that VHE γ -rays are naturally produced by the EIC+SSC mechanism, which may provide an explanation for the observation of VHE γ -rays from GRB 190829A by H.E.S.S.. The EIC scenario is seeded by the observed long-lasting late-prompt flare in the X-ray and optical bands as target photons. Assuming that the nonthermal electrons are accelerated in the external forward shock, these can upscatter the late-prompt flare photons, and our results show that the EIC components can contribute to the H.E.S.S. observations at $t \sim 1 \times 10^4$ s.

We consider an impulsive relativistic outflow propagating into an external medium with a constant density, where the physical parameters adopted in this work are optimized for fitting the multiwavelength light curve. We showed that our model can explain the multiwavelength observations of GRB 190829A, given $\mathcal{E}_k = 10^{52}$ erg, $\Gamma_0 = 25$, and $n_{\text{ex}} \sim 0.1 \text{ cm}^{-3}$. Our results suggest that GRB 190829A is not a typical LL GRB but has much higher kinetic energy. The TeV photons observed by H.E.S.S. can be dominated by EIC emission at earlier times, while the SSC component becomes dominant at later times. Our results suggest that the EIC emission nearly coincides with the late-prompt flare, but decreases more slowly than the evolution of the flare emission, and extends ~ 3 – 4 times longer than the duration of the flare emission. Future observations of EIC components that are related to late-prompt flares in GRBs will be helpful for constraining the properties of the outflow and central engine activities.

The work of K.M. is supported by the Alfred P. Sloan Foundation, NSF grant No. AST-1908689, and KAKENHI No. 20H01901 and No. 20H05852. B.T.Z. acknowledges the IGC fellowship. P.M. acknowledges support from the Eberly Foundation. P.V. acknowledges support from NASA grants 80NSSC19K0595 and NNM11AA01A.

Appendix

We calculate time-dependent spectra of high-energy afterglow emission by extending the method used in Murase et al. (2011). We numerically calculate afterglow dynamics to treat not only the relativistic regime (described by the self-similar solution) but also the nonrelativistic regime, and take into account effects of EATS.

Appendix A Afterglow Dynamics

We consider an impulsive relativistic outflow with kinetic energy \mathcal{E}_k and initial Lorentz factor Γ_0 , propagating into an external medium of constant density n_{ex} . The total energy of the blast wave that develops is given by Nava et al. (2013)

$$\mathcal{E}_{\text{tot}} = \Gamma M_{\text{ej}} c^2 + \Gamma m c^2 + \frac{\hat{\gamma} \Gamma^2 - \hat{\gamma} + 1}{\Gamma} \mathcal{E}'_{\text{int}}, \quad (\text{A1})$$

where $M_{\text{ej}} = \mathcal{E}_k / \Gamma_0 c^2$ is the mass of the outflow, $m = (4\pi/3)r^3 n_{\text{ex}} m_p$ is the mass of the swept-up external matter, $\hat{\gamma} = (4 + \Gamma^{-1})/3$ is the adiabatic index, which is a good approximation in both relativistic and nonrelativistic regimes

(Nava et al. 2013). The comoving internal energy is $\mathcal{E}'_{\text{int}} = (\Gamma - 1)mc^2$. Considering $d\mathcal{E}'_{\text{tot}} = dmc^2$ and neglecting both adiabatic and radiative energy losses (see Nava et al. 2013; Zhang 2018, for details), we can derive the following 1D differential equation,

$$\frac{d\Gamma}{dm} = -\frac{\Gamma - 5\Gamma^3 + 4\Gamma^5}{3M_{\text{ej}}\Gamma^3 - 2m + 8\Gamma^4 m}. \quad (\text{A2})$$

The differential mass of the collected external medium is $dm = 4\pi r^2 n_{\text{ex}} f_{\text{corr}} m_p dr$. We can derive the well-known relation $\Gamma \propto r^{-2/3}$ once the blast wave enters into the Blandford–McKee (BM) self-similar adiabatic evolution regime (Blandford & McKee 1976). Note that we multiply a factor of $f_{\text{corr}} = 9/17$ to the swept-up external matter density in order to match the normalization of the BM self-similar solution (Nava et al. 2013). The BM self-similar phase begins after a significant deceleration occurs, where the kinetic energy of the initial ejecta equals the sum of the kinetic energy of the swept-up external matter and its internal energy $\Gamma M_{\text{ej}} c^2 \sim \hat{\gamma} \Gamma^2 m c^2$. In order to obtain the value of quantities in the observer frame, we adopt the differential relation, $dr = \beta c dt / (1 - \beta)$, which represents the case that photons propagate with distance dr can be observed in a time interval dt . The differential equation derived in Equation (A2) also gives an appropriate description of the blast wave evolution in both the coasting ($\Gamma = \Gamma_0$, $r \propto t$) and nonrelativistic deceleration ($\beta \propto t^{-3/5}$, $r \propto t^{2/5}$) regimes (Huang et al. 1999; Panaitescu & Kumar 2000; Pe’er 2012; Nava et al. 2013; Lu et al. 2020).

Appendix B Nonthermal Electron Distribution

We calculate afterglow synchrotron and SSC spectra numerically, and we confirm that the numerical results agree with the analytical results. In general, electron energy spectra in the downstream of the external forward shock can be derived by solving the kinetic equation (Blumenthal & Gould 1970),

$$\frac{\partial n_{\gamma_e}(t')}{\partial t'} + \frac{\partial}{\partial \gamma_e} (n_{\gamma_e}(t') \dot{\gamma}_e) + \frac{n_{\gamma_e}(t')}{t'_{\text{esc}}} = \dot{n}_{\gamma_e}^{\text{inj}}(t'), \quad (\text{B1})$$

where $n_{\gamma_e}(t')$ is the number density of electrons per electron Lorentz factor, $\dot{\gamma}_e = d\gamma_e/dt' = \gamma_e t'^{-1}_{\text{cool}}$ is the electron energy loss rate (divided by $m_e^2 c^2$), t'_{esc} is the possible escape time, $\dot{n}_{\gamma_e}^{\text{inj}}(t') = \mathcal{C} \gamma_e^{-s}$ is the electron injection rate where $\mathcal{C} \approx (s - 1) \gamma_{e,m}^{s-1} n_e / t'_{\text{dyn}}$ (for $s > 2$), $\gamma_{e,m}$ is the electron minimum Lorentz factor, n_e is the nonthermal electron number density in the comoving frame, which is normalized based on

$N_e = 4\pi r^2 n_e t'_{\text{dyn}} c = (4\pi/3) r^3 n_{\text{ex}} f_e$, and considering an on-axis observer we use $t'_{\text{dyn}} \approx \Gamma t / (1 + z)$ as the dynamical timescale. The electron minimum Lorentz factor is given by $\gamma_{e,m} \approx (\epsilon_e/f_e)[(s-2)/(s-1)](m_p/m_e)(\Gamma-1)$ for $s > 2$, where ϵ_e is the energy fraction of thermal energy that goes into nonthermal electrons and f_e is the number fraction of thermal electrons that are injected into the acceleration process. The total cooling rate consists of radiative cooling and possible adiabatic losses. The synchrotron loss rate is $t'^{-1}_{\text{syn}} = (4/3) \sigma_T c (\gamma_e/m_e c^2) \beta^2 U_B$, where $U_B = B^2/8\pi$ is the magnetic energy density (Rybicki et al. 1986). The IC loss rate t'^{-1}_{IC} is implemented as in Equation (B3) of Murase et al. (2011), which includes both SSC and EIC processes. The adiabatic loss rate is $t'^{-1}_{\text{ad}} \sim t'^{-1}_{\text{dyn}}$. In general, the electron distribution is obtained by solving the above differential equation in a time-dependent manner. We call this method “numerical, time-dependent”, but we demonstrate the results using $t'_{\text{esc}} = t'_{\text{dyn}}$, by which we approximately take into account adiabatic energy losses or particle escape after the decay of magnetic fields in the downstream. The steady-state solution via $\partial n_{\gamma_e} / \partial t' = 0$ can also be found as in Equation (C.11) in Dermer & Menon (2009). On the other hand, for results presented in the main text, we take the iteration method as in Murase et al. (2011). However, different from the previous work that calculated $\gamma_{e,c}$ with analytical synchrotron spectra and used broken power-law electron distributions, we determine the electron distribution using numerical synchrotron spectra through the following function,

$$n_{\gamma_e}(t') = \frac{1}{t'^{-1}_{\text{dyn}} + t'^{-1}_{\text{cool}}} \frac{1}{\gamma_e} \int d\gamma'_e \dot{n}_{\gamma'_e}(t'). \quad (\text{B2})$$

This function is motivated by the steady-state solution for $t'^{-1}_{\text{cool}} = t'^{-1}_{\text{syn}} + t'^{-1}_{\text{IC}} + t'^{-1}_{\text{ad}}$ in the no escape limit. In the fast-cooling case, the electron distribution is mostly described by the steady-state distribution for $t'^{-1}_{\text{cool}} = t'^{-1}_{\text{syn}} + t'^{-1}_{\text{IC}}$. In the slow cooling case, it is essentially the injection distribution with spectral steepening by radiative cooling. This method was also used in Asano et al. (2020) and Zhang et al. (2021). In Figure B1, we compared the electron energy spectrum derived using the iteration method mentioned above and the spectrum via numerically solving the time-dependent kinetic Equation (B1).

For comparison, we will also show analytical afterglow synchrotron and SSC spectra, and this method is called “analytical”, where $\gamma_{e,c}$ is determined by the iteration method to evaluate the Compton Y parameter.

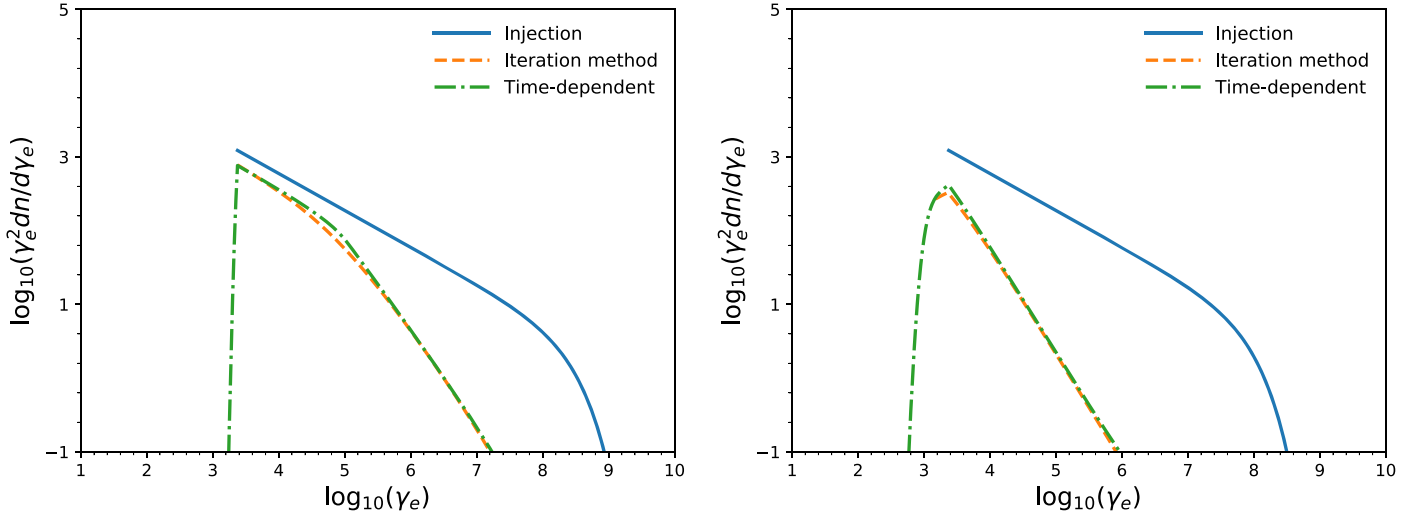


Figure B1. Comparison of the electron energy spectra derived by the iteration method used for the main results and by solving the kinetic equation at $t' = 100$ s. We use $\mathcal{E}_k = 1 \times 10^{52}$ erg, $n_{\text{ex}} = 1 \text{ cm}^{-3}$, $\epsilon_e = 0.3$, $f_e = 1.$, $s = 2.5$, $\Gamma_0 = 50$. Left panel: slow cooling regime, $\epsilon_B = 10^{-3}$. Right panel: fast-cooling regime, $\epsilon_B = 10^{-1}$.

Appendix C Radiative Processes

The observed radiation flux from a relativistically moving object can be derived via integration over the EATS (e.g., Granot et al. 1999; Woods & Loeb 1999)

$$F_E(t) = \frac{1+z}{d_L^2} \int_0^{2\pi} d\phi \int_{-1}^1 d\mu \int_0^\infty dr r^2 \frac{j_{e'}(\epsilon', \Omega', \hat{t}, r)}{\Gamma^2(1 - \beta \cos \theta)^2}, \quad (\text{C1})$$

where z is the source redshift, d_L is the luminosity distance of the source, $j_{e'}(\epsilon', \Omega', \hat{t}, r)$ is the comoving emissivity at r and time \hat{t} , $\mu = \cos \theta$, Γ is the Lorentz factor. The observation time is $t = (1+z)(\hat{t} - r\mu/c)$, where we assume $t = 0$ is the arrival time of photon emitted at origin at $\hat{t} = 0$. We assume instantaneous emission at \hat{t}_i , $j_{e'} = j_{e'} \delta(\hat{t} - \hat{t}_i) \Delta \hat{t}_i = j_{e'} \delta(\hat{t} - \hat{t}_i)(r_i/\beta c \Gamma)$. Using the relation $\delta(\hat{t} - \hat{t}_i) = \delta(\hat{\mu} - \hat{\mu}_i)c/r_i$, Equation (C1) can be simplified as

$$F_E(t) = \frac{(1+z)2\pi}{d_L^2} \int_0^\infty dr r^2 \frac{j_{e'}(\epsilon', r, \hat{t})}{\Gamma^3 \beta (1 - \beta \cos \theta)^2}. \quad (\text{C2})$$

The comoving synchrotron emissivity can be calculated using the following formula,

$$j_{e'}^{\text{syn}} = \frac{\sqrt{3}}{4\pi} \frac{e^3 B}{m_e c^2 2\pi \hbar \epsilon'} \int d\gamma_e n_{\gamma_e} G(x), \quad (\text{C3})$$

where

$$G(x) \approx \frac{1.81 e^{-x}}{(x^{-2/3} + (3.62/\pi)^2)^{1/2}}, \quad (\text{C4})$$

$x = \epsilon'/\epsilon'_c$ and $\epsilon'_c = (3e\hbar B/2m_e c)\gamma_e^2 \beta^2$ is the critical energy (Rybicki et al. 1986; Aharonian et al. 2010).

The comoving SSC emissivity is estimated to be

$$j_{e'}^{\text{SSC}} = \frac{3}{16\pi} \sigma_T c \int d\gamma_e \frac{1}{\gamma_e^2} n_{\gamma_e} \int d\epsilon'_{\text{syn}} \frac{\epsilon'}{\epsilon'_{\text{syn}}} \frac{dn'_{\text{syn}}}{d\epsilon'_{\text{syn}}} f(q, w), \quad (\text{C5})$$

where σ_T is the Thomson cross section, $dn'_{\text{syn}}/d\epsilon'_{\text{syn}}$ is the comoving synchrotron photon density, and

$$f(q, w) = 2q \ln q + (1+2q)(1-q) + \frac{1}{2} \frac{(wq)^2}{1+wq} (1-q), \quad (\text{C6})$$

$q = \epsilon'/(4\gamma_e \epsilon'_{\text{syn}})(\gamma_e - \epsilon'/m_e c^2)$, and $w = 4\epsilon'_{\text{syn}} \gamma_e/m_e c^2$ (Blumenthal & Gould 1970). Note the Thomson limit corresponds to $w \ll 1$, while the above expression is valid for the value of w as long as $\gamma_e \gg 1$ (Blumenthal & Gould 1970).

The comoving EIC emissivity can be calculated as

$$j_{e'}^{\text{EIC}} = \frac{3}{8\pi} \sigma_T c (1 - \cos \theta'_{\text{sc}}) \int d\gamma_e n_{\gamma_e} \int dy A(y) \epsilon'_{\text{ph}} \frac{dn'_{\text{ph}}}{d\epsilon'_{\text{ph}}}, \quad (\text{C7})$$

where ϵ' is the comoving EIC photon energy, ϵ'_{ph} is the comoving seed photon energy, $dn'_{\text{ph}}/d\epsilon'_{\text{ph}}$ is the comoving density of seed photons, θ'_{sc} is the scattering angle measured in the forward shock comoving frame relative to the direction of the photon beam, $y \equiv \xi m_e c^2 / (2(1 - \cos \theta'_{\text{sc}}) \gamma_e \epsilon'_{\text{ph}} (1 - \xi))$, $\xi \equiv \epsilon' / (\gamma_e m_e c^2)$, and $A(y) \equiv (1 - \xi)[1 - 2y + 2y^2 + \xi^2 / (2(1 - \xi))]$ (Aharonian & Atoyan 1981; Toma et al. 2009; Murase et al. 2011). Assuming the direction of the photon beam at the scattering point following the radial expansion of the jet, the observed flux can be evaluated at $\theta'_{\text{sc}} = \theta'$ in the jet comoving frame where $\cos \theta'_{\text{sc}} = \cos \theta' = (\mu - \beta) / (1 - \beta\mu)$ with $\mu = \cos \theta$.

In Figure C1, left, we compare results of different methods for the single-zone model. The iteration method used in this work agrees with the method of solving the time-dependent equation. Both of the numerical results agree with the analytical formula. The analytical synchrotron and SSC spectra are taken from Murase et al. (2011), where the BM solution with $r = 4\Gamma^2 ct$ is used for dynamics (Blandford & McKee 1976; Waxman 1997; Sari et al. 1998) and the synchrotron peak flux is evaluated with a correction factor introduced in Wijers & Galama (1999). Note that the SSC spectrum in the Thomson

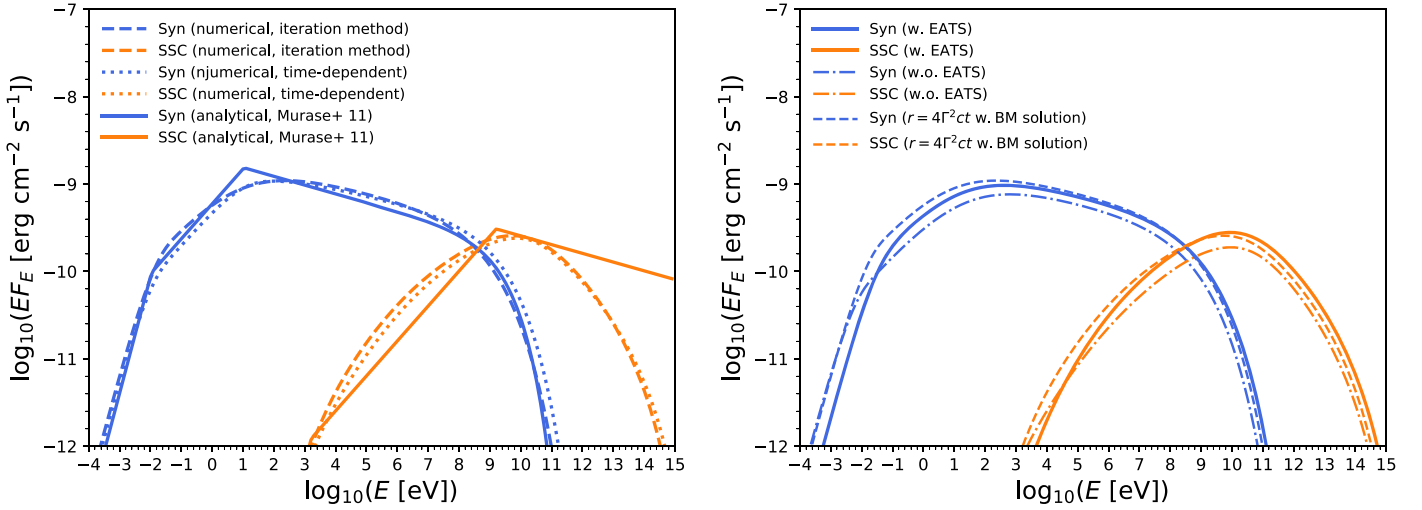


Figure C1. Left panel: comparison of energy spectra of synchrotron and SSC emission at $t = 10^4$ s calculated in the single-zone model with both the numerical method (solid line) and the analytical method (dotted-dashed line). The dotted line is calculated by the numerical method with a time-dependent electron energy spectrum via solving Equation (B1). We also use the relation $r = 4\Gamma^2 ct$ in this panel. Right panel: comparison of energy spectra of synchrotron and SSC emission at $t = 10^4$ s calculated with EATS (solid line) and without EATS (dotted-dashed line) using the detailed dynamics described in Appendix A. The dashed line is calculated by the single-zone model using the same dynamics as in the left panel. The relevant physical parameters are $\mathcal{E}_k = 1 \times 10^{53}$ erg, $n_{\text{ex}} = 1 \text{ cm}^{-3}$, $\epsilon_e = 0.05$, $f_e = 1$, $\epsilon_B = 1 \times 10^{-2}$, $s = 2.2$, $\Gamma_0 = 100$, and $z = 0.0785$.

limit is shown here, although Murase et al. (2011) also considered spectral suppression due to the Klein–Nishina effect analytically. In Figure C1, right, we compare results of the single-zone model with $r = 4\Gamma^2 ct$ to those of the detailed afterglow dynamics model with/without EATS. This panel demonstrates that the detailed model with EATS agrees with the standard single-zone afterglow model in the relativistic limit, although our detailed method has an advantage that it can be used for both relativistic and nonrelativistic regimes consistently. Note that our synchrotron energy spectra calculated with EATS are also consistent with the results of Granot & Sari (2002).

Photons with energy beyond the pair production threshold will undergo internal absorption by ambient photons inside the source and external absorption by extragalactic background light (EBL) during their propagation to Earth. The threshold energy can be estimated from the kinematic condition, $\epsilon' \epsilon'_{\text{seed}} \gtrsim (m_e c^2)^2$, where ϵ' is the comoving high-energy photon energy and ϵ'_{seed} is the comoving target photon energy. As in Murase et al. (2011), we use the $\gamma\gamma$ optical depth,

$$\tau_{\gamma\gamma} = \frac{\tilde{\Delta}}{2} \int_{-1}^1 d\mu (1 - \mu) \int d\epsilon'_{\text{seed}} \frac{dn}{d\epsilon'_{\text{seed}}} \sigma_{\gamma\gamma}(S), \quad (\text{C8})$$

where

$$\sigma_{\gamma\gamma}(S) = \frac{3}{16} \sigma_T \left(1 - \beta_{\text{cm}}^2 \right) \left[\left(3 - \beta_{\text{cm}}^4 \right) \ln \left(\frac{1 + \beta_{\text{cm}}}{1 - \beta_{\text{cm}}} \right) - 2\beta_{\text{cm}} \left(2 - \beta_{\text{cm}}^2 \right) \right] \quad (\text{C9})$$

is the two-photon annihilation cross section, $\beta_{\text{cm}} = \sqrt{1 - 4S^{-1}}$, and $S = 2\epsilon'_{\text{seed}} \epsilon' (1 - \mu)$ is the Mandelstam variable. Here, $\tilde{\Delta}$ is the comoving width, and the attenuation at a given EATS includes from contributions with different values of $\tilde{\Delta}$. For simplicity, we adopt $\tilde{\Delta} \approx ct/(1 + z)$ and ignore effects of electromagnetic cascades. The photon spectrum after the

internal $\gamma\gamma$ absorption can be estimated as $F_E^{\gamma\gamma} = F_E/(1 + \tau_{\gamma\gamma})$. The EBL is mainly composed of infrared and optical photons, and we use the low-IR model calculated in Kneiske et al. (2004). The observed energy spectrum is

$$F_E^{\text{ob}} = F_E^{\gamma\gamma} e^{-\tau_{\gamma\gamma}^{\text{EBL}}(E, z)}, \quad (\text{C10})$$

where $\tau_{\gamma\gamma}^{\text{EBL}}(E, z)$ is the optical depth at given observed photon energy $E = \epsilon/(1 + z)$ and redshift z .

ORCID iDs

B. Theodore Zhang <https://orcid.org/0000-0003-2478-333X>
 Kohta Murase <https://orcid.org/0000-0002-5358-5642>
 Péter Veres <https://orcid.org/0000-0002-2149-9846>
 Péter Mészáros <https://orcid.org/0000-0002-4132-1746>

References

- Abdalla, H., Adam, R., Aharonian, F., et al. 2019, *Natur*, 575, 464
 Abdalla, H., Aharonian, F., Ait Benkhali, F., et al. 2021, *Sci*, 372, 1081
 Acciari, V. A., Ansoldi, S., Antonelli, L. A., et al. 2019a, *Natur*, 575, 455
 Acciari, V. A., Ansoldi, S., Antonelli, L. A., et al. 2019b, *Natur*, 575, 459
 Aharonian, F., & Atoyan, A. 1981, *Ap&SS*, 79, 321
 Aharonian, F. A., Kelner, S. R., & Prosekin, A. 2010, *PhRvD*, 82, 43002
 Ando, S., & Mészáros, P. 2008, *ApJ*, 689, 351
 Asano, K., & Mészáros, P. 2008, *ApJ*, 677, L31
 Asano, K., Murase, K., & Toma, K. 2020, *ApJ*, 905, 105
 Blandford, R., & Eichler, D. 1987, *PhR*, 154, 1
 Blandford, R. D., & McKee, C. F. 1976, *PhFl*, 19, 1130
 Blumenthal, G. R., & Gould, R. J. 1970, *RvMP*, 42, 237
 Brunetti, G. 2000, *Aph*, 13, 107
 Campana, S., Mangano, V., Blustin, A. J., et al. 2006, *Natur*, 442, 1008
 Chand, V., Banerjee, A., Gupta, R., et al. 2020, *ApJ*, 898, 42
 de Naurois, M. 2019, ATel, 13052, 1
 Derishev, E., & Piran, T. 2019, *ApJL*, 880, L27
 Dermer, C. D., Chiang, J., & Mitman, K. E. 2000, *ApJ*, 537, 785
 Dermer, C. D., & Menon, G. 2009, High Energy Radiation from Black Holes: Gamma Rays, Cosmic Rays and Neutrinos (Princeton, USA: Princeton U. Pr.)
 Drury, L. 1983, *RPPh*, 46, 973
 Evans, P. A., Willingale, R., Osborne, J. P., et al. 2010, *A&A*, 519, A102
 Fan, Y., Piran, T., Narayan, R., et al. 2008, *MNRAS*, 384, 1483
 Fraija, N., Dichiaro, S., Pedreira, A. C., et al. 2019, *ApJ*, 885, 29

- Fraija, N., Veres, P., Beniamini, P., et al. 2021, *ApJ*, **918**, 12
- Galama, T., Vreeswijk, P. M., van Paradijs, J., et al. 1998, *Natur*, **395**, 670
- Granot, J., Piran, T., & Sari, R. 1999, *ApJ*, **513**, 679
- Granot, J., & Sari, R. 2002, *ApJ*, **568**, 820
- He, H.-N., Wang, X.-Y., Yu, Y.-W., & Mészáros, P. 2009, *ApJ*, **706**, 1152
- He, H.-N., Zhang, B.-B., Wang, X.-Y., Li, Z., & Mészáros, P. 2012, *ApJ*, **753**, 178
- Hinton, J. A., & Hofmann, W. 2009, *ARA&A*, **47**, 523
- Hu, Y.-D., Castro-Tirado, A. J., Kumar, A., et al. 2021, *A&A*, **646**, A50
- Huang, Y. F., Dai, Z. G., & Lu, T. 1999, *MNRAS*, **309**, 513
- Inoue, S., Granot, J., O'Brien, P. T., et al. 2013, *Aph*, **43**, 252
- Kashiyama, K., Murase, K., Horiuchi, S., Gao, S., & Meszaros, P. 2013, *ApJL*, **769**, L6
- Kimura, S. S., Murase, K., Ioka, K., et al. 2019, *ApJL*, **887**, L16
- Kneiske, T. M., Bretz, T., Mannheim, K., & Hartmann, D. H. 2004, *A&A*, **413**, 807
- Kulkarni, S. R., Frail, D. A., Wieringa, M. H., et al. 1998, *Natur*, **395**, 663
- Kumar, P., & Zhang, B. 2014, *PhR*, **561**, 1
- Lemoine, M. 2013, *MNRAS*, **428**, 845
- Liu, R.-Y., Wang, X.-Y., & Wu, X.-F. 2013, *ApJL*, **773**, L20
- Lu, W., Beniamini, P., & McDowell, A. 2020, arXiv:2005.10313
- Marcello, G. 2021, Black Hole Astrophysics with VLBI: Multi-Wavelength and Multi-Messenger Era (Tokyo: Univ. Tokyo)
- Mészáros, P. 2006, *RPPH*, **69**, 2259
- Mészáros, P., Fox, D. B., Hanna, C., & Murase, K. 2019, *NatRP*, **1**, 585
- Mészáros, P., & Rees, M. J. 1994, *MNRAS*, **269**, L41
- Murase, K. 2012, *ApJL*, **745**, L16
- Murase, K., & Bartos, I. 2019, *ARNPS*, **69**, 477
- Murase, K., & Beacom, J. F. 2010, *PhRvD*, **82**, 043008
- Murase, K., Ioka, K., Nagataki, S., & Nakamura, T. 2008, *PhRv*, **D78**, 23005
- Murase, K., Toma, K., Yamazaki, R., & Mészáros, P. 2011, *ApJ*, **732**, 77
- Murase, K., Toma, K., Yamazaki, R., Nagataki, S., & Ioka, K. 2010, *MNRAS*, **402**, L54
- Murase, K., Toomey, M. W., Fang, K., et al. 2018, *ApJ*, **854**, 60
- Nakar, E., Ando, S., & Sari, R. 2009, *ApJ*, **703**, 675
- Nava, L., Sironi, L., Ghisellini, G., Celotti, A., & Ghirlanda, G. 2013, *MNRAS*, **433**, 2107
- Norris, J. P., Bonnell, J. T., Kazanas, D., et al. 2005, *ApJ*, **627**, 324
- Panaiteescu, A., & Kumar, P. 2000, *ApJ*, **543**, 66
- Panaiteescu, A., & Mészáros, P. 1998, *ApJL*, **493**, L31
- Pe'er, A. 2012, *ApJL*, **752**, L8
- Rhodes, L., van der Horst, A. J., Fender, R., et al. 2020, *MNRAS*, **496**, 3326
- Rybicki, G. B., Lightman, A. P., & Paul, A. G. 1986, *Astron. Nachr.*, **307**, 170
- Samuelsson, F., Bégué, D., Ryde, F., Pe'er, A., & Murase, K. 2020, *ApJ*, **902**, 148
- Sari, R., & Esin, A. A. 2001, *ApJ*, **548**, 787
- Sari, R., Piran, T., & Narayan, R. 1998, *ApJL*, **497**, L17
- Sato, Y., Obayashi, K., Yamazaki, R., Murase, K., & Ohira, Y. 2021, *MNRAS*, **504**, 5647
- Soderberg, A. M., Kulkarni, S. R., Nakar, E., et al. 2006, *Natur*, **442**, 1014
- Toma, K., Wu, X.-F., & Mészáros, P. 2009, *ApJ*, **707**, 1404
- Valeev, A. F., Castro-Tirado, A. J., Hu, Y. D., et al. 2019, *GCN*, 25565, 1
- Vanthieghem, A., Lemoine, M., Plotnikov, I., et al. 2020, *Galax*, **8**, 33
- Veres, P., & Mészáros, P. 2012, *ApJ*, **755**, 12
- Wang, X.-Y., He, H.-N., Li, Z., Wu, X.-F., & Dai, Z.-G. 2010, *ApJ*, **712**, 1232
- Wang, X.-Y., Li, Z., & Meszaros, P. 2006, *ApJL*, **641**, L89
- Wang, X.-Y., Liu, R.-Y., Zhang, H.-M., Xi, S.-Q., & Zhang, B. 2019, *ApJ*, **884**, 117
- Wang, X.-Y., & Mészáros, P. 2006, *ApJL*, **643**, L95
- Waxman, E. 1997, *ApJ*, **491**, L19
- Wijers, R. A. M. J., & Galama, T. J. 1999, *ApJ*, **523**, 177
- Woods, E., & Loeb, A. 1999, *ApJ*, **523**, 187
- Zhang, B. 2018, *The Physics of Gamma-Ray Bursts* (Cambridge: Cambridge Univ. Press)
- Zhang, B., Fan, Y. Z., Dyks, J., et al. 2006, *ApJ*, **642**, 354
- Zhang, B., & Mészáros, P. 2001, *ApJ*, **559**, 110
- Zhang, B. T., Murase, K., Yuan, C., Kimura, S. S., & Mészáros, P. 2021, *ApJL*, **908**, L36
- Zhang, H., Christie, I., Petropoulou, M., Rueda-Becerril, J. M., & Giannios, D. 2020, *MNRAS*, **496**, 974